International Journal of Heat and Mass Transfer 57 (2013) 567–581

Contents lists available at SciVerse ScienceDirect

International Journal of Heat and Mass Transfer

journal homepage: www.elsevier.com/locate/ijhmt

Experimental measurement and modeling of downflow condensation in a circular tube

Ilchung Park, Sung-Min Kim, Issam Mudawar *

Boiling and Two-Phase Flow Laboratory (BTPFL), Purdue University International Electronic Cooling Alliance (PUIECA), Mechanical Engineering Building, 585 Purdue Mall, West Lafayette, IN 47907-2088, USA

ARTICLE INFO

Article history:
Received 1 April 2012
Received in revised form 16 October 2012
Accepted 18 October 2012
Available online 23 November 2012

Keywords:
Condensation
Downflow
Annular flow
Eddy diffusivity

ABSTRACT

This study explores the interfacial and heat transfer characteristics of annular condensation of FC-72 in vertical downflow. Two separate condensation test modules are employed, one for high-speed video imaging of the film interface and the second for heat transfer measurements. Condensation in both test modules is achieved by rejecting the heat to a counterflow of cooling water. The heat transfer measurements are obtained along the inner wall of an 11.89-mm i.d. and 1259.84-mm long stainless steel tube. For very low FC-72 flow rates, the film is observed to be both smooth and laminar. The film turns turbulent with a very wavy interface as the flow rate of FC-72 is increased, especially for exit film Reynolds numbers above 1800. The heat transfer coefficient decreases axially because of a gradual thickening of the liquid film. However, the data show a downstream minimum before the heat transfer coefficient increases again towards the outlet as the film transitions to turbulent flow, enhanced by the more intense downstream waves. A control-volume-based model is proposed, which incorporates an eddy diffusivity profile for the liquid film that accounts for interfacial dampening of turbulence due to surface tension. The model shows good accuracy in predicting the average condensation heat transfer coefficient data, evidenced by a mean absolute error of 12.59%.

1. Introduction

Condensers are thermal devices found in numerous industries, including power generation, food, pharmaceutical and space. They also constitute one of the primary components of any refrigeration or air conditioning system. Recently, increased power densities in modern electronic and power devices have created the need for specialized phase-change thermal management systems to tackle both the heat acquisition from the device by boiling, and the heat rejection to the ambient by condensation. These applications include high performance computers, electrical vehicle power electronics, avionics, and directed energy laser and microwave weapon systems [1,2]. Proposed thermal management systems for these applications include boiling modules that rely on a variety of configurations, including spray [3–5], jet [6–9], and micro-channel cooling schemes [2,10–13], as well as techniques to enhance surface micro-structure [14]. Unfortunately, far less emphasis has been placed on the heat rejection, or condenser part of these systems.

Condensers come in a wide variety of designs. Some rely on gravity to drive the condensate liquid, while, in most, the condensate is shear-driven by the vapor flow. Shell-and-tube designs involve condensation of vapor along the outer walls of parallel horizontal tubes, while vertical condensers rely on condensation along multiple vertical tubes.

Formation of the liquid film has a strong bearing on the performance of any condenser. In fact, the high condensation heat transfer coefficients realized in condensers are the direct result of the transport behavior of the liquid film. For very thin films, heat transfer across the film is dominated by pure conduction, while thicker films also benefit from turbulent eddies.

For condensation in tubes, the flow is introduced in mostly vapor state. With a wall temperature smaller than the saturation temperature of the vapor, heat is transferred to the wall by gradually transforming the vapor into liquid. A succession of flow regimes is possible, starting with the annular flow regime, where a thin liquid film is formed along the wall, driven mostly by the shear forces exerted by the vapor core. The film is initially very thin but grows gradually in thickness. This gradually thickening, aided by the formation of interfacial waves, ultimately leads to bridging of liquid films across the vapor core and formation of slug flow. In the slug flow regime, the oblong bubbles gradually decrease in length and are replaced by a dispersion of smaller bubbles, which are characteristic of the bubbly regime. Finally, a pure liquid flow regime is established as all remaining vapor is converted into liquid.

* Corresponding author. Tel.: +1 765 494 5705; fax: +1 765 494 0539.
E-mail address: mudawar@ecn.purdue.edu (I. Mudawar).
URL: https://engineering.purdue.edu/BTPFL (I. Mudawar).

0017-9310/$ - see front matter © 2012 Elsevier Ltd. All rights reserved.
http://dx.doi.org/10.1016/j.ijheatmasstransfer.2012.10.060

Nomenclature

A	area
A^+	constant in eddy diffusivity function
$A_{f,*}$	flow area of liquid control volume
c_p	specific heat at constant pressure
D	diameter
f_i	interfacial friction factor
G	mass velocity
g	gravitational acceleration
h	condensation heat transfer coefficient; enthalpy
$\bar{h}$	condensation heat transfer coefficient averaged over region where $x < 1$
h_{fg}	latent heat of vaporization
K	Von-Karman constant
k_{ss}	thermal conductivity of inner stainless steel tube
MAE	mean absolute error
$\dot{m}_f$	mass flow rate of FC-72 liquid film
$\dot{m}_{FC}$	total mass flow rate of FC-72
$\dot{m}_w$	total mass flow rate of cooling water
P	pressure
P_f	perimeter
Pr	Prandtl number
Pr_T	turbulent Prandtl number
q	heat transfer rate
q''	heat flux at distance y from inner wall of inner stainless steel tube
q''_w	heat flux at inner wall of inner stainless steel tube
q_w	total heat transfer rate from FC-72 to cooling water
Re_f	FC-72 film Reynolds number, $Re_f = G(1-x)D_h/\mu_f$
T	temperature
T^+	dimensionless temperature
u	velocity
u_f	local liquid film velocity
u^+	dimensionless liquid film velocity
u^*	friction velocity
x	mass quality
x_e	thermodynamic equilibrium quality
y	distance perpendicular to inner wall of inner stainless steel tube
y^+	dimensionless distance perpendicular to inner wall of inner stainless steel tube
z	stream-wise distance

Greek symbols

Γ_{fg}	rate of mass transfer due to condensation
δ	thickness of condensing film
δ^+	dimensionless film thickness
ε_m	eddy momentum diffusivity
μ	dynamic viscosity
ν	kinematic viscosity
ρ	density
σ	surface tension
τ	shear stress
τ_w	shear stress at inner wall of inner stainless steel tube

Subscripts

c	vapor core
exp	experimental, measured
f	saturated liquid; liquid film
FC	FC-72
g	saturated vapor; vapor core
i	interfacial; inner wall of inner stainless steel tube
in	inlet
o	outer wall of inner stainless steel tube
out	outlet
$pred$	predicted
sat	saturation
w	water; wall
$wall$	wall of inner stainless steel tube

The annular flow regime is perhaps the most important condensation regime, given that this regime contributes the highest heat transfer coefficients as well as tends to occupy a significant fraction of the tube length in most practical condensing systems. This explains the greater emphasis investigators place on modeling this regime compared to all other condensation regimes.

Studies on annular condensation in tubes have resulted in different approaches to predicting the condensation heat transfer coefficient. The vast majority of authors rely on the use or development of semi-empirical correlations [15–26]. A key limitation of the semi-empirical approach is limited validity to only the parameter ranges of the database upon which a correlation is based. "Universal" correlations applicable to many fluids and very broad ranges of operating conditions, including pressures approaching the critical point, are very few. Researchers at the Purdue University Boiling and Two-Phase Flow Laboratory (PU-BTPFL) have developed universal correlations for a number of important two-phase flow configurations, including flow boiling critical heat flux [27–30] and, more recently, pressure drop in horizontal, adiabatic mini/micro-channels [31], and condensation heat transfer coefficient in horizontal mini/micro-channels [32]. However, these universal correlations can be developed for a given two-phase flow or heat transfer configuration only after a very comprehensive database for the same configuration is amassed and made available to the heat transfer community at large.

An alternative to the use of limited range correlations or universal correlations is the control volume approach, where conservation models are applied separately to the liquid film and vapor core. Investigators at PU-BTPFL have successfully used this approach to model a variety of two-phase flow configurations, including pool boiling [33,34], and vertical separated flow boiling along short walls [35,36] and long heated walls [37–40]. Recently, they also used the control volume approach to construct a new model for annular condensation in horizontal mini/micro-channel flows [41]. The success of the control volume approach is the primary reason behind adopting the same approach in the present study.

The validity of any predictive model is highly dependent on its effectiveness in capturing the underlying physical mechanisms. This is especially the case with thin film flows, where transport behavior is complicated by the influence of surface tension forces on turbulent eddies in the film [41–46], and by interfacial waves [47,48]. Unfortunately, these complicating features require very complex simultaneous measurements of film thickness [47–49], interfacial wave shape and speed [47,48], and flow field [48], which are not possible with very thin films.

The present study will address the transport behavior of downflow annular condensation using FC-72 as working fluid. A condensation facility is developed to achieve annular flow in a vertical circular tube by rejecting heat to a counterflow of cooling water. Two separate condensation modules are employed, one for flow visualization and the second for heat transfer measurements. Using the flow visualization module, high-speed video imaging and photomicrographic techniques are used to track the axial development of interfacial waves. The second condensation module is used to measure the axial variation of the condensation heat transfer coefficient for different flow rates of both the FC-72 and

the cooling water. A control-volume-based model of the annular flow is developed, which accounts for the dampening effects of surface tension on turbulence in the annular liquid film. The model predictions of the average condensation heat transfer coefficient are compared to the measured values.

2. Experimental methods

2.1. Condensation flow loop

The condensing fluid selected for this study is FC-72, a 3M-company perfluorinated fluid that is clear, colorless and odorless. It is also inert, non-toxic, non-flammable and highly dielectric. It has a moderate boiling point of 56 °C at atmospheric pressure, and a latent heat and surface tension one order of magnitude smaller than those for water. Table 1 provides representative thermophysical properties of FC-72 at 60 °C, which is the saturation temperature corresponding the average operating pressure for the present study.

Fig. 1a shows a schematic of the condensation facility constructed for the present study. The facility consists of a primary loop for the condensing fluid, FC-72, and two secondary water cooling loops. Heat is transferred from the primary loop to the first water loop via the condensation module, which constitutes the primary test section for the facility. Heat is also transferred from the primary loop to the second water cooling loop via a separate condenser. Fig. 1b shows a photo of the entire facility.

In the primary loop, FC-72 liquid contained in sealed reservoir is circulated through the primary loop with the aid of a gear pump. The liquid is first passed through one of several rotameters connected in parallel for flow rate measurement. The liquid is then passed through a 14.2 kW Watlow Cast-X 3000 pre-heater, where it is converted to vapor. The pre-heater is fitted with a PID temperature controller to ensure that the FC-72 exits the pre-heater in slightly superheated state. The FC-72 temperature is measured at the inlet to the pre-heater, and both the FC-72 temperature and pressure are measured at the inlet to the condensation module. These measurements, along with the measured electrical heat input to the pre-heater, are used to determine the FC-72 vapor mass quality at the inlet to the condensation module. The superheated FC-72 vapor then enters the condensation module where is gradually converted to liquid by rejecting heat to a counter-flow of water from the first secondary water loop. The FC-72 temperature and pressure are measured once more at the exit of the condensation module. Exiting the condensation module, the FC-72 passes through a plate-type condenser, where it is cooled by the second water cooling loop, followed by an air-cooled condenser to bring any vapor exiting the test module to sub-cooled liquid state before returning to the reservoir.

The first water cooling loop consists of a 14-kW modular Lytron LCS cooling system and water rotameters. The Lytron system consists of a water reservoir, water pump and a liquid-to-liquid heat exchanger; the heat exchanger is used to reject the heat absorbed by the water from the FC-72 to enable precise temperature control of the water as it enters the condensation module. The water temperature and pressure are measured both at the inlet and exit of the condensation module.

Condensation of the FC-72 in the second water cooling loop is achieved via a plate-type condenser, by rejecting heat to water that is circulated by a 1.46-kW modular Lytron MCS cooling system. This second Lytron system consists of a water reservoir, pump and water-to-air heat exchanger; the latter is used to reject the heat to ambient air.

Two separate systems are used to rid the FC-72 from any dissolved non-condensable gases prior to performing any tests. The first is a vacuum pump that is used initially to remove any non-condensables by creating vacuum inside the system. The second is an air-cooled condenser. To assist the deaeration process, the reservoir of the primary loop is fitted with two 300-W immersion heaters to produce vigorous boiling in the FC-72 liquid. A mixture of vapor and non-condensable gases is passed through the deaeration condenser, where most of the vapor is recaptured by condensation as the non-condensable gases are purged to the ambient.

2.2. Condensation module for flow visualization

Two separate condensation modules were constructed for this study, one for flow visualization purposes and the other for heat transfer measurements. The two condensation modules have similar geometries, but are constructed from different materials to suit their specific purposes.

Fig. 2 illustrates the construction of the condensation module intended for flow visualization. The module features a transparent tube-in-tube construction with the FC-72 flowing downwards through the inner tube, and the water flowing in counterflow (upwards) through the annulus between the inner and outer tubes. To enable viewing of the interfacial behavior of the condensing FC-72 film, the inner 1219-mm-long tube is made from borosilicate glass with a 10.16-mm i.d. and a wall thickness of 1.8 mm. The outer tube is made from polycarbonate plastic (Lexan), which, like the inner tube, features high transparency but possesses a much lower thermal conductivity. The outer tube has an i.d. of 19.05 mm and an o.d. of 25.4 mm. The inner tube is secured at both ends inside the outer tube with the aid of short latex rubber sleeves, leaving a condensation length of 1143 mm for flow visualization. The condensation module is instrumented to measure the temperatures and pressures of the FC-72 and the cooling water at the inlet and the exit of the condensation module. Type-T thermocouples and pressure transducers are used to measure temperature and pressure, respectively, of the FC-72 both at the inlet and outlet. For the waterside, type-T thermocouples and liquid-filled pressure gauges are used to measure temperature and pressure, respectively, both at the inlet and outlet.

2.3. Flow visualization methods

Flow visualization is achieved with the aid of high-speed video imaging and photomicrographic techniques. A Photron Fastcam Ultima APX video camera system, capable of shutter speeds up to 1/120,000 s, is used in conjunction with an assortment of Infinity K2/SC long-distance microscope lenses. This system provides the necessary combination of fast shutter speed and high magnification required to capture the interfacial behavior of the condensing FC-72 liquid film with high resolution.

The camera is placed normal to the front of the condensation module. The high shutter speed requires intense back lighting, which is provided by an incandescent bulb. Even lighting of the photographed region is achieved with the aid of a diffuse film that

Table 1
Thermophysical properties of saturated FC-72 at 60 °C (P = 1.135 bar).

k_f (W/m K)	μ_f (kg/m s)	$c_{p,f}$ (J/kg K)	σ (mN/m)	h_f (kJ/kg)	h_{fg} (kJ/kg)	ρ_f (kg/m^3)	ρ_g (kg/m^3)
0.0534	418×10^{-6}	1107	8.02	99.67	93.69	1583	14.90

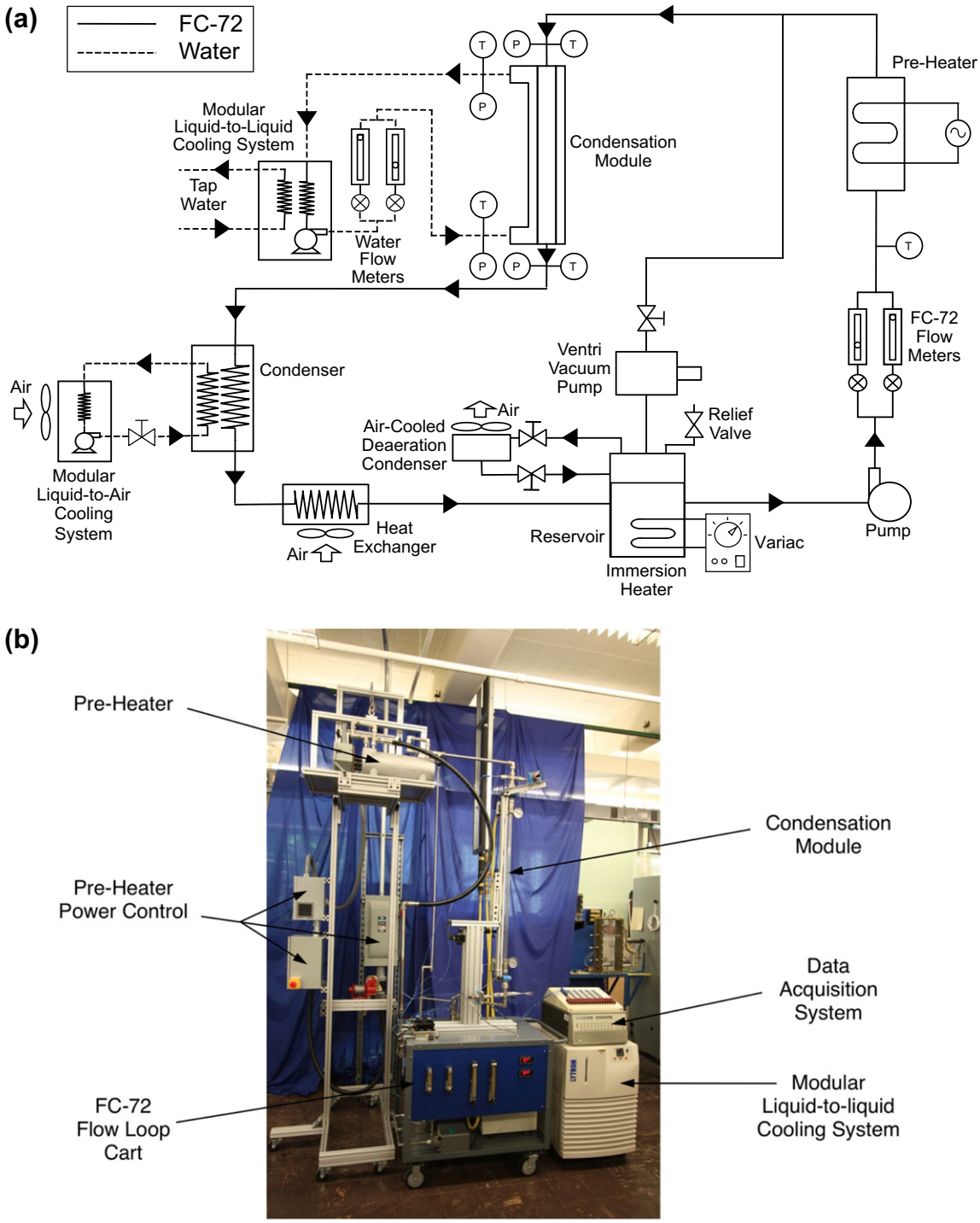

Fig. 1. (a) Schematic diagram of test loop. (b) Photo of test facility.

is situated between the light source and the condensation module. Flow visualization is performed at three different locations centered at 190, 571, and 952 mm from the inlet of the inner tube corresponding to the inlet, middle, and outlet regions, respectively. Each captured region is approximately 381-mm long.

2.4. Condensation module for heat transfer measurements

As indicated earlier, the overall design of the condensation module intended for heat transfer measurements is very similar to that for flow visualization as shown in Fig. 2a. However, different materials are used for the second condensation module to facilitate accurate heat transfer measurements.

Illustrated in Fig. 3a, the condensation module for heat transfer measurements uses inner and outer tubes made from 304 stainless steel. The inner tube has an i.d. of 11.89 mm and a wall thickness of 0.41 mm, while the outer tube has an i.d. of 22.48 mm with a 3.05-mm wall thickness. The total condensation length of this module is 1259.84 mm. A key goal with this construction is to achieve a compromise between minimizing the resistance to radial heat conduction between the condensing film and the water, and minimizing axial wall conduction effects along the direction of fluid flow. This

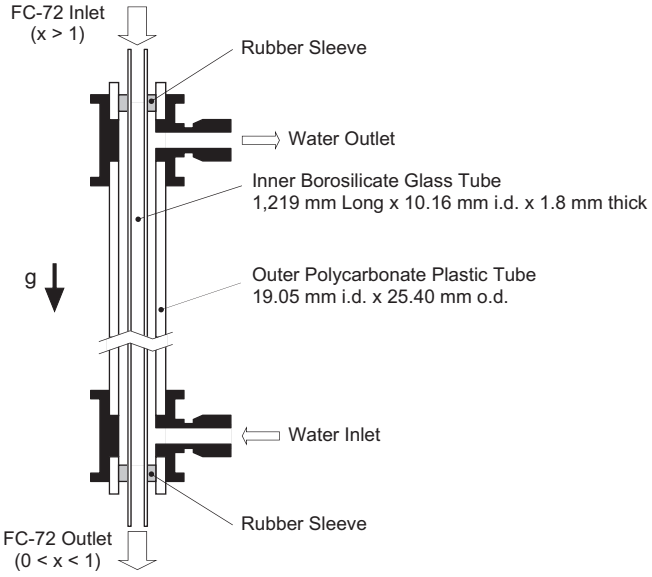

Fig. 2. Construction of condensation module for flow visualization studies.

compromise is achieved by the combination of small thickness of the inner tube and relatively low thermal conductivity of the stainless steel wall.

Aside from utilizing the same temperature and pressure instrumentation at the FC-72 and water inlets and outlets as the flow visualization module, the second module contains 45 additional type-T thermocouples. As illustrated in Fig. 3b, 28 of these thermocouples are attached to the outer surface of the inner tube to measure the local surface temperatures in 14 diametrically opposite pairs. Use of thermocouple pairs is intended to detect any asymmetry in the wall temperature. Fig. 4 shows the inner tube's outer wall temperatures measured on opposite sides for three sets of operating conditions. The maximum difference between diametrically opposite thermocouples is 0.94 °C, proving the condensation module design ensured symmetry in the film flow.

There are also 14 thermocouples exposed to the water flow in the annulus at the same axial locations as the wall thermocouples, in addition to 3 thermocouples for the water flow measurement diametrically opposite to 3 of the 14 main water thermocouples, again to assess any asymmetry in water temperatures. All thermocouples are made from 0.21-mm thermocouple diameter wire with a bead diameter of 0.79 mm. The thermocouples are fitted along 1.57-mm diameter stainless steel tubes.

To capture the sharp axial variations of wall temperature near the inlet with greater resolution, the axial distance between thermocouples is smallest in the FC-72 inlet region, 38.1 mm, and increases down the length of the condensation module to 76.2 mm and 139.7 mm in the middle and exit regions, respectively. To minimize heat loss to the ambient, the module is wrapped with a thick layer of fiberglass insulation.

2.5. Operating conditions and measurement uncertainty

Two series of experiments are performed using the two aforementioned condensation modules. The first is intended to capture the interfacial behavior of the condensing film at three axial locations about 381-mm long inlet, middle and outlet regions, which are centered at axial locations of 190, 571 and 952 mm, respectively. The second series of tests is dedicated to heat transfer measurements that span the entire length of the condensation module. For both series of tests, efforts are made to maintain the thermodynamic equilibrium quality, x_e, of FC-72 at the inlet slightly above unity to maintain annular flow over the entire length of each condensation module.

The flow visualization series of tests consists of a matrix of 40 operating conditions that are summarized in Table 2. These tests cover five different mass flow rates of FC-72 ($\dot{m}_{FC} = 1.56, 3.12, 3.62, 7.30$, and 11.07 g/s) and 8 water flow rates ($\dot{m}_w = 1.74, 2.03, 5.72, 8.58, 11.44, 14.31, 17.17$, and 20.03 g/s). The inlet quality, temperature and pressure of FC-72 range from $x_{e,in}$ = 1.00–1.03, $T_{FC,in}$ = 55.56–66.93 °C and $P_{FC,in}$ = 133.89–171.93 kPa, respectively. Aside from the inlet temperature and pressure of FC-72, the amount of heat transferred from the condensing FC-72 vapor to the cooling water is dictated by the water flow rate; the heat transfer rate for the flow visualization tests varies from 154.38 to 536.38 W. This corresponds to variations of FC-72 thermodynamic equilibrium quality and FC-72 film Reynolds number at the outlet of $x_{e,out}$ = 0–0.8 and $\mathrm{Re}_{f,out}$ = 355.54–1741.82, respectively.

The test matrix for the heat transfer measurements consists of 56 operating conditions that are summarized in Table 3. These tests cover seven mass flow rates of FC-72 ($\dot{m}_{FC} = 20.48, 25.58, 30.63, 35.63, 40.74, 45.76$, and 50.85 g/s) and eight water flow rates; the water flow rate ranges from 49.1% to 163.1% of each FC-72 flow rate. Only heat transfer data measured over the upstream condensation length of z = 0–807.7 mm are used in the present study to avoid any uncertainty in determining the FC-72 heat transfer coefficient due to cooling water entrance effects. The inlet quality of FC-72 is maintained in the range of $x_{e,in}$ = 1.04–1.08 for all cases, which corresponds to a single-phase superheated vapor inlet region 21.0–59.8-mm long (2.6–7.4% of the 807.7 mm length considered in the heat transfer measurements). For the two-phase condensation region ($x_e \leqslant 1$), the ranges of outlet quality of FC-72 and rate of heat transfer from FC-72 to the cooling water are $x_{e,out}$ = 0.45–0.74 and q_w = 636.25–2721.27 W, respectively.

For both condensation modules, FC-72 pressures and temperatures are measured by absolute pressure transducers and type-T thermocouples, respectively, both at the inlet and outlet. The measurements are made after all system pressures and temperatures reach steady state. The data are processed by an HP-3852A data acquisition system.

Measurement uncertainties are ±0.5% for the pressure transducers and ±3.0% for the flow meters for both FC-72 and cooling water. All thermocouples used in the present study have uncertainties less than ±0.03 °C. This relatively low uncertainty is achieved by careful calibration using ice water and boiling water. During these calibration tests, thermocouples are typically off their mean values by ±0.03 °C, and the offset for each thermocouple is corrected using the HP-3852A data acquisition system. Geometric uncertainties of the condensing tube used in the heat transfer measurements are ±0.08 mm and ±0.03 mm for outer diameter and wall thickness, respectively. The uncertainties of the outer diameter and wall thickness of the outer tube of the same condensation module are ±0.13 mm and ±0.18 mm, respectively. Considering all these uncertainties along with the uncertainties associated with determination of thermophysical properties from the measured pressures and temperatures, the overall uncertainties in determining the rate of heat transfer from FC-72 to the cooling water, vapor quality, and condensation heat transfer coefficient are ±5.76%, ±6.20%, and ±6.23%, respectively.

3. Flow visualization results

Before discussing the flow visualization results, it is important to point out a key limitation of the optical techniques used in conjunction with the flow visualization module. Because the FC-72 film covers the entire inner wall of the inner tube, the captured

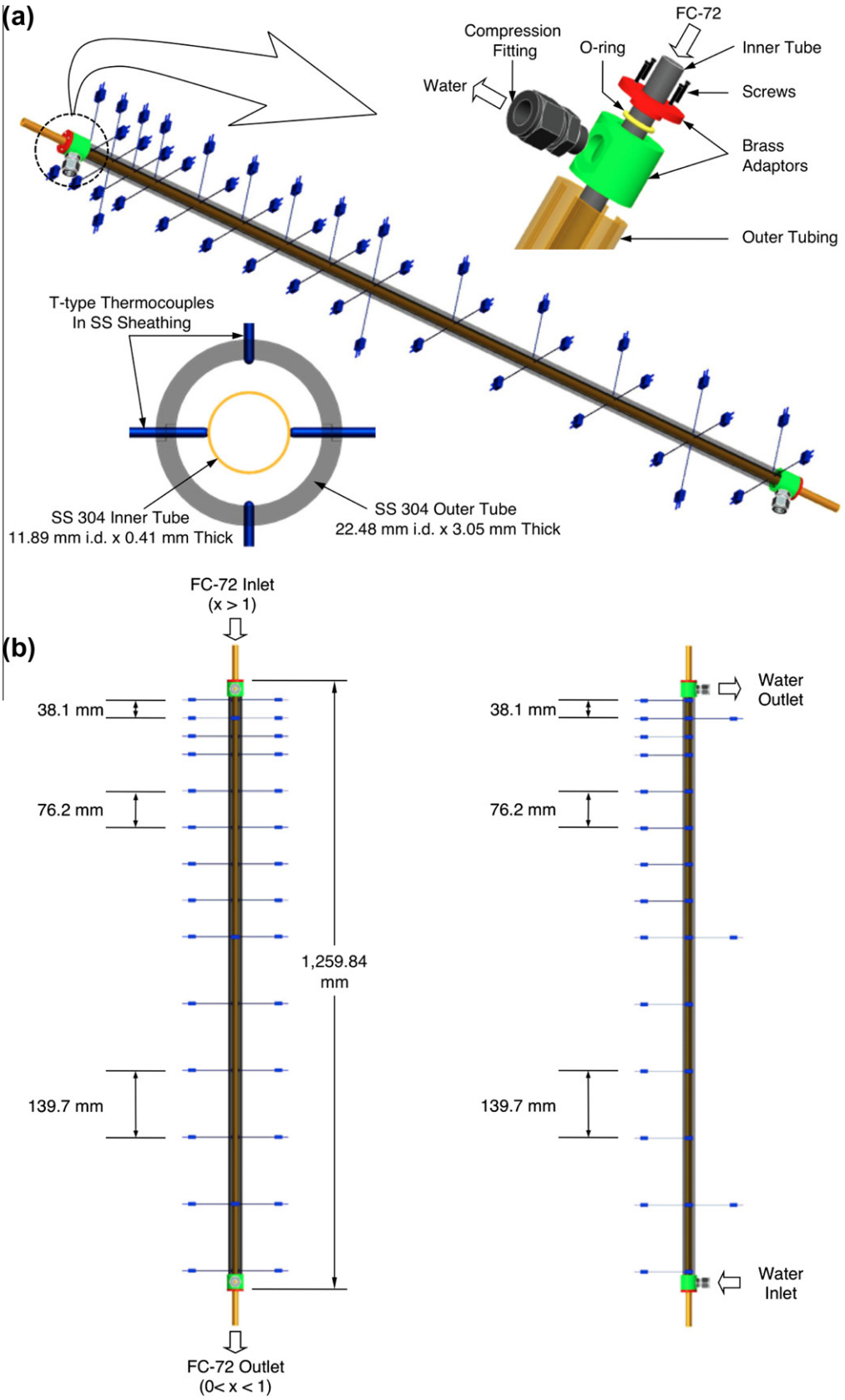

Fig. 3. (a) Construction of condensation module for heat transfer measurements. (b) Locations of thermocouples for inner tube and water flow measurements.

video images represent those of two separate interfaces overlaid on one another. This hinders any detailed quantitative assessment of the interfacial structure of the film. Nonetheless, the vast differences captured in video provide important inferences concerning the influence of individual parameters on the film's transport behavior.

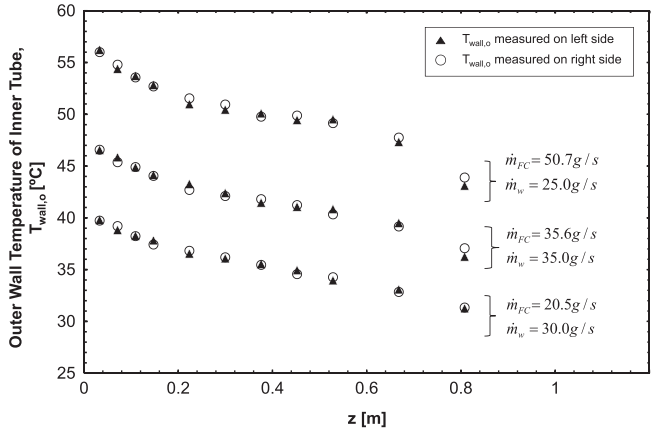

Fig. 4. Variations of measured left and right outer wall temperatures of inner tube with axial distance.

Fig. 5 shows representative photos of the film interface obtained using the flow visualization module for five different flow rates of FC-72 and a constant water flow rate of 5.72 g/s (G_w = 28.05 kg/m^2 s). Increasing $\dot{m}_{FC}$ produces higher interfacial shear as well as more turbulence, which, in turn, influence interfacial instabilities of the condensing film. This is evidenced by the photos corresponding to the three lower values of $\dot{m}_{FC}$ appearing relatively smooth and laminar, marred only by a few surface ripples. On the other hand, those for the two highest values of $\dot{m}_{FC}$ are far more turbulent with the interface incurring more chaotic interfacial waviness. Both the film flow rate and corresponding film Reynolds number, Re_f, increase along the flow direction as vapor is gradually being converted into liquid, and reach maximum values at the outlet. The influence of these axial increases is manifest in Fig. 5 in the form of increased turbulence and interfacial waviness towards the outlet, especially for the two highest values of $\dot{m}_{FC}$. Overall, predominantly laminar flow is maintained for outlet Reynolds numbers up to $Re_{f,out}$ = 770.

Fig. 6 shows representative images for four different water flow rates and a constant FC-72 inlet flow rate of FC-72 of $\dot{m}_{FC}$ = 3.62 g/s (G_{FC} = 44.65 kg/m^2 s). Fig. 6 shows the same overall trends in interfacial behavior relative to axial position as depicted in Fig. 5. Here too, the film appears to turn more turbulent and the waves more chaotic as the film thickens axially along the tube. Increasing the water flow rate increases the amount of heat extracted from the condensing FC-72 vapor, which hastens the condensation process and thickening of the condensation film. This is manifest in the higher water flow rates further increasing both the turbulence and film waviness.

4. Heat transfer measurements

4.1. Heat transfer data reduction

A thermal model is constructed to determine the local condensation heat transfer coefficient. Fig. 7 shows all the relevant parameters for a control volume of axial length Δz. Ignoring axial conduction effects along the wall of the inner tube, a differential amount of heat, dq, is transferred from the FC-72 to the cooling water, which is also equal to the differential rise in sensible energy of the cooling water. The film interface is maintained at $T_{sat}(z)$, which is determined from the pressure measurements, given that the measure pressure drop was very small for all operating conditions. The saturation pressure, $P_{sat}(z)$, used to determine $T_{sat}(z)$ is determined from a linear curve fit between the measured inlet pressure, P_{in} (which is assumed equal to local saturation pressure at the end of the short superheated region) and outlet pressure, P_{out}. The water temperature, $T_w(z)$, and outer wall temperature of the inner tube, $T_{wall,o}(z)$, are determined from curve fits to their respective measured values.

The thermal model for the region where $x_e < 0$ is represented by the relation:

$$dq = (\pi D_i\, dz)h(T_{sat} - T_{wall,i}) = \frac{T_{wall,i} - T_{wall,o}}{\frac{\ln(D_o/D_i)}{2\pi k_{ss} dz}} = \dot{m}_w c_{p,w} dT_w, \tag{1}$$

which is used to determine the local condensation heat transfer coefficient, $h(z)$, of FC-72.

For the small superheated inlet region before the liquid film begins to develop, the temperature of the superheated FC-72 vapor, $T_g(z)$, may be determined from the simple energy balance:

$$\dot{m}_{FC} c_{p,g} dT_g = \dot{m}_w c_{p,w} dT_w. \tag{2}$$

The thermodynamic equilibrium quality for vapor in the superheated region is given by:

$$x_e = 1 + \frac{c_{p,g}(T_g - T_{sat})}{h_{fg}}. \tag{3}$$

Eq. (3) can is also used to determine the location where x_e = 0. To determine the heat transfer coefficient for the superheated region, Eq. (1) is modified by replacing T_{sat} with the local temperature of the superheated vapor:

$$dq = (\pi D_i\, dz)h(T_g - T_{wall,i}) = \frac{T_{wall,i} - T_{wall,o}}{\left[\frac{\ln(D_o/D_i)}{2\pi k_{ss} dz}\right]} = \dot{m}_w c_{p,w} dT_w. \tag{4}$$

For the saturated region (x_e < 1), the local flow rate of the condensing film, $\dot{m}_f(z)$, can be obtained by integrating the relation

Table 2
Experimental operating conditions for the flow visualization study.

	FC-72					Cooling water			q_w (W)	$x_{e,out}$	$Re_{f,out}$
	$x_{e,in}$	$\dot{m}_{FC}$ (g/s)	$G_{FC\text{-}72}$ (kg/m^2 s)	$T_{FC,in}$ (°C)	$P_{FC,in}$ (kPa)	$\dot{m}_w$ (g/s)	G_w (kg/m^2 s)	ΔT_w (°C)			
Max	1.03	11.07	136.54	66.93	171.93	20.03	98.21	30.06	536.4	0.80	1741.82
Min	1.00	1.56	19.24	55.56	133.89	1.74	8.53	2.87	154.4	0	355.54

Table 3
Experimental operating conditions for the condensation heat transfer data.

	FC-72					Cooling water			q_w (W)	$x_{e,out}$	$Re_{f,out}$
	$x_{e,in}$	$\dot{m}_{FC}$ (g/s)	G_{FC} (kg/m^2 s)	$T_{FC,in}$ (°C)	$P_{FC,in}$ (kPa)	$\dot{m}_w$ (g/s)	G_w (kg/m^2 s)	ΔT_w (°C)			
Max.	1.08	50.85	457.97	86.58	209.88	83.27	291.29	15.78	2721.3	0.74	6400.56
Min.	1.04	20.48	184.45	63.43	108.57	9.99	34.95	7.48	636.2	0.45	1315.54

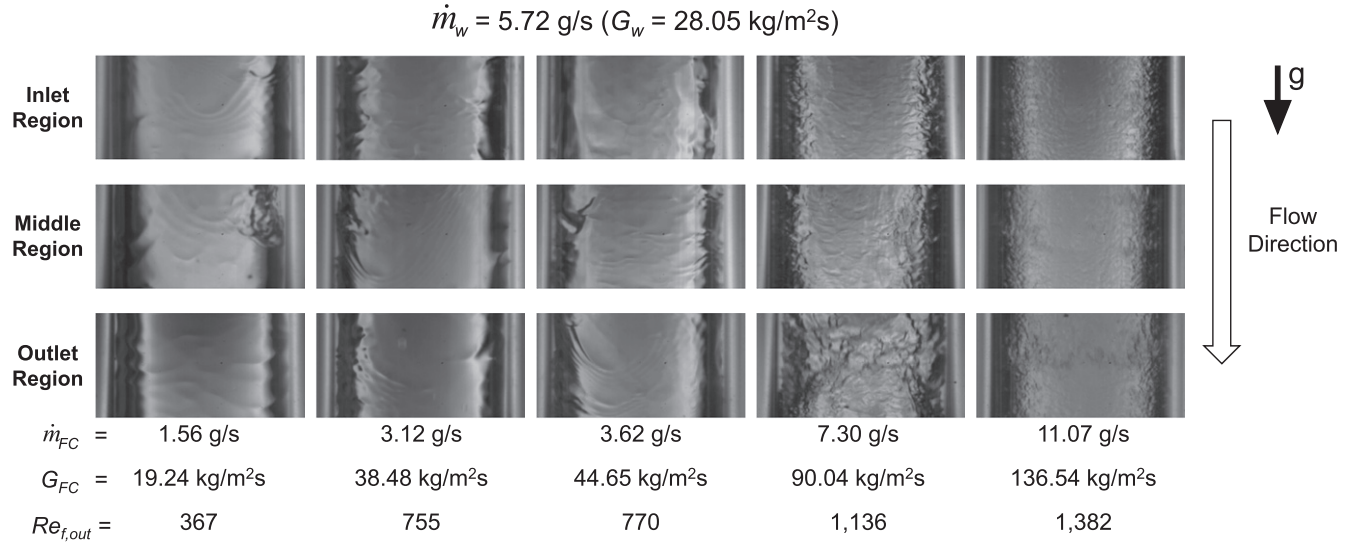

Fig. 5. Photos of condensation film in inlet, middle and outlet regions of flow visualization module for different FC-72 flow rates and a fixed water flow rate of $\dot{m}_w = 5.72$ g/s ($G_w = 28.05$ kg/m^2 s).

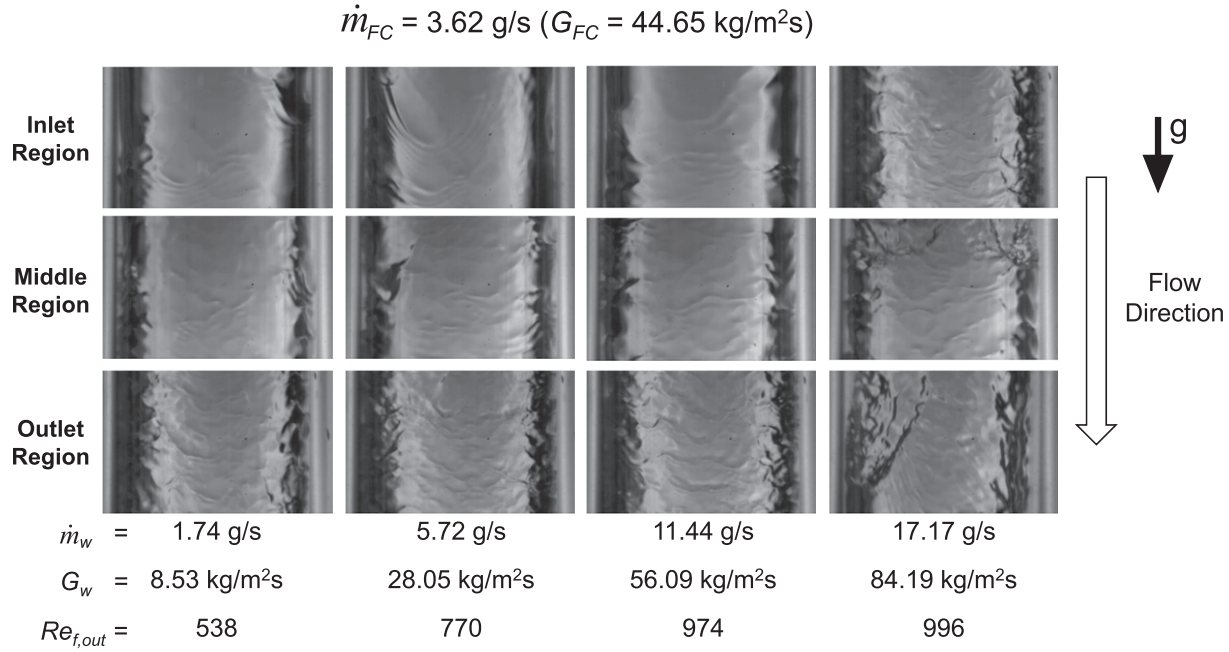

Fig. 6. Photos of condensation film in inlet, middle and outlet regions of flow visualization module for different water flow rates and a fixed FC-72 flow rate of $\dot{m}_{FC} = 3.62$ g/s ($G_{FC} = 44.65$ kg/m^2 s).

$$d\dot{m}_f = \frac{dq}{h_{fg}} \tag{5}$$

from the location where $x_e = 0$. The local mass quality of vapor in the same region is given by

$$x = \frac{\dot{m}_{FC} - \dot{m}_f}{\dot{m}_{FC}}. \tag{6}$$

4.2. Heat transfer results

Fig. 8a illustrates, for four different FC-72 flow rates and a constant water flow rate of $\dot{m}_w = 33.3$ g/s ($G_w = 116.49$ kg/m^2 s), how the axial variations of the outer wall temperature of the inner tube, $T_{wall,o}$, and the cooling water temperature, $T_w(z)$, are determined from the thermocouple measurements. Both temperature distributions are determined from third-order-polynomial curve fits to axial distance. These distributions are then used to calculate the corresponding variations of the amount of heat transferred from FC-72 to the cooling water per unit length, dq/dz, using Eqs. (1) and (4), and the FC-72 mass quality, x, using Eq. (6). As shown in Fig. 8b for each of the four FC-72 flow rates, dq/dz is highest in the upstream region where the condensate film is thinnest, and decreases gradually towards the middle of the condensation module because of the increase in film thickness. An increase in dq/dz towards the outlet may be explained by increases in both turbulence and interfacial waviness as shown earlier in Figs. 5 and 6. Notice that dq/dz also increases with increasing FC-72 flow rate because

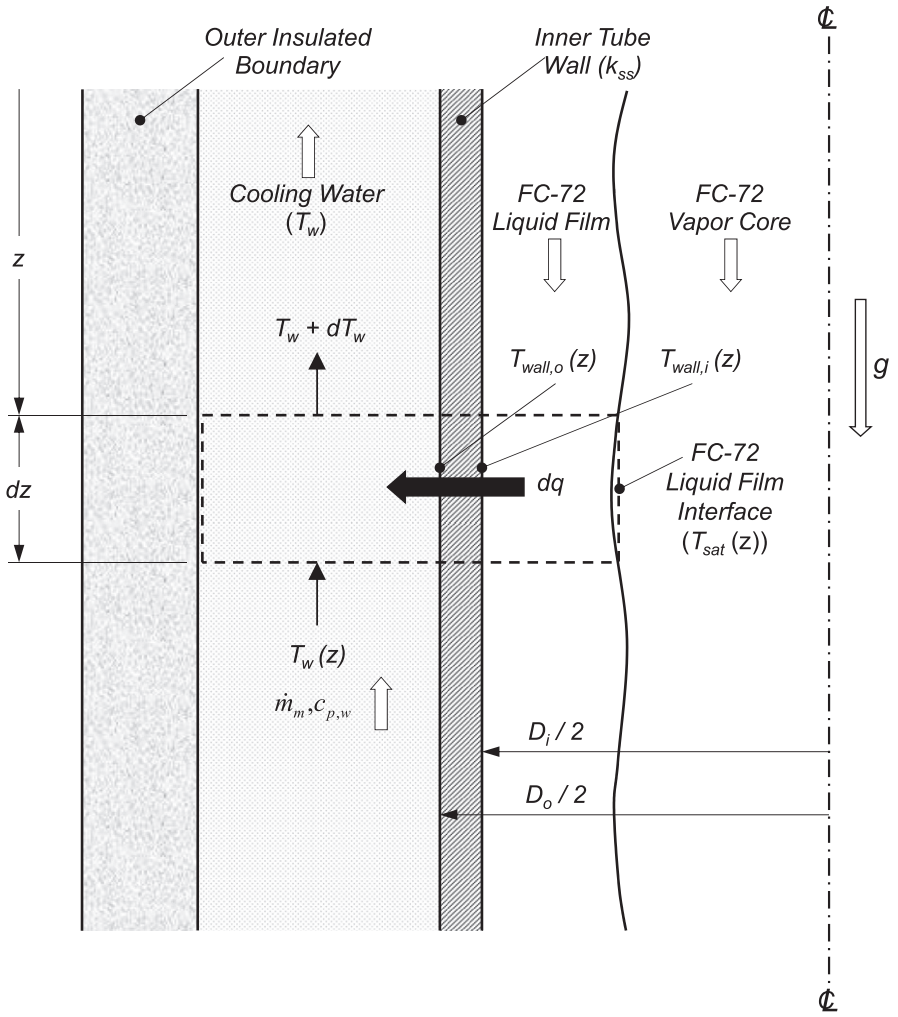

Fig. 7. Thermal model used to determine the condensation heat transfer coefficient for FC-72.

of the higher condensation heat transfer coefficient resulting from the increased vapor shear.

Fig. 9a–c shows the variations of the experimentally determined local FC-72 heat transfer coefficient with axial distance in both the single-phase superheated vapor and film condensation regions for different water mass flow rates and FC-72 mass flow rates of 20.48, 30.63 and 45.76 g/s (G_{FC} = 184.45, 275.86, and 412.13 kg/m^2 s), respectively. The local heat transfer coefficient in the superheated vapor region near the inlet is relatively low for most cases. The heat transfer coefficient increases rather sharply to its peak value where the annular liquid film is initiated and is very thin. One unexpected trend is the increase in h upstream of the peak point since single-phase vapor flow should yield a fairly constant h value. This may be explained by the film condensation commencing partially within the predominantly single-phase vapor region where $x_e > 1$ over a portion of the inner tube circumference. The peak value is believed to occur where full coverage of the inner circumference by the liquid film is achieved. Fig. 9a–c shows the expected trend of decreasing h along the inner tube due to gradual thickening of the liquid film. However, the data show h reaches a minimum before increasing again towards the outlet. Since the liquid film continue to thicken in the downstream region, it is believed heat transfer in the downstream region is no longer dominated by conduction across the film. As suggested by the photos of the film in Figs. 5 and 6, two possible reasons for the downstream increase are (a) transition from laminar to turbulent flow and (b) heat transfer enhancement due to the more intense downstream waviness. Fig. 9a–c shows, for a fixed $\dot{m}_{FC}$, h generally decreases with increasing $\dot{m}_w$ towards the peak point but increases downstream. This trend may be explained by the larger $\dot{m}_w$ increasing the cooling rate and, therefore, contributing to a thickening of the film, which, for the upstream region that is dominated by conduction, tends to decrease h. However, the increase in cooling rate precipitates both an earlier transition to turbulent flow and an increase in turbulence overall, which explains the downstream enhancement with increasing $\dot{m}_w$. Comparing data between Fig. 9a–c shows increasing $\dot{m}_{FC}$ for a fixed $\dot{m}_w$ produces an increase in h, which can be explained by the larger $\dot{m}_{FC}$ values increasing vapor shear and therefore contributing to a thinning of the film. Fig. 10a–c shows corresponding variations of h with vapor quality, x. These plots, which exclude the region captured in Fig. 9a–c from the inlet to the peak point, show an initial monotonic decline in h due to increasing film thickness in a predominantly laminar film, followed by an increase in h downstream because of the transition to turbulent flow and increased waviness.

Fig. 11 shows the variation of the average condensation heat transfer coefficient, $\bar{h}$, with water flow rate for different FC-72 mass flow rates. The values presented here and in subsequent plots are averaged over the annular flow region downstream of the peak locations in Fig. 9, therefore excluding the upstream superheated vapor region. Fig. 11 shows an initial decrease in $\bar{h}$ with increasing $\dot{m}_w$ for the lower mass flow rates of FC-72 ($\dot{m}_{FC} = 20.48, 25.58,$

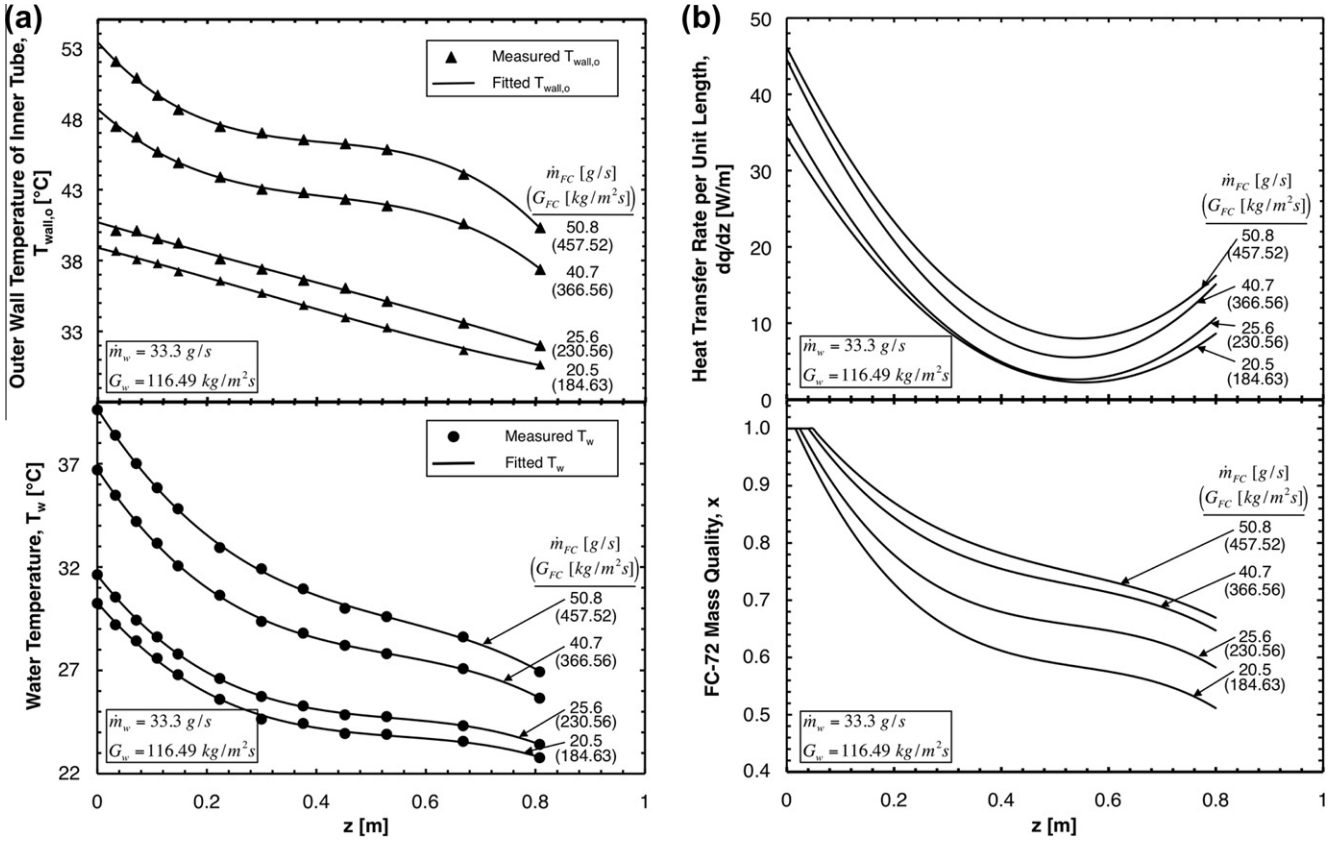

Fig. 8. Axial variations of (a) measured and fitted outer wall temperature of inner tube and cooling water temperature and (b) amount of heat transferred from FC-72 to the cooling water per unit distance and mass quality of FC-72 for four different FC-72 mass flow rates with a water flow rate of 33.3 g/s (G_w = 116.49 kg/m² s).

30.63 and 35.63 g/s), brought about by a thickening of the upstream laminar liquid film due to a faster cooling rate. But the trend is reversed once the film turns turbulent, where the benefits of increased turbulence and intensity of the interfacial waves outweigh the drawbacks of the increased film thickness. Fig. 11 also shows a monotonic increase in $\bar{h}$ with increasing $\dot{m}_{FC}$ because of the increasing magnitude of vapor shear exerted on the film.

Fig. 12 shows the variation of $\bar{h}$ with exit film Reynolds number. There is an initial decrease in $\bar{h}$ with $Re_{f,out}$ for $Re_{f,out}$ < 1800 corresponding to predominantly laminar, heat-conduction-dominated condensation. Above $Re_{f,out}$ = 1800, $\bar{h}$ begins to increase monotonically because of the afore-mentioned dominance of turbulent flow, assisted by interfacial waviness.

5. Condensation model

5.1. Control volume analysis

Recently, Kim and Mudawar [41] examined the pressure drop and heat transfer characteristics for annular condensation of FC-72 in square horizontal micro-channels. They developed a theoretical control-volume-based model based on the assumptions of smooth interface between the annular liquid film and vapor core, and uniform film thickness around the channel's circumference. Since the present study concerns condensation in vertical downflow, a theoretical model similar to that of Kim and Mudawar is adopted, which is modified to incorporate the influence of gravity.

Following the solution procedure of Kim and Mudawar, mass and momentum conservation are applied to control volumes encompassing a portion of the liquid film and the vapor core as illustrated in Fig. 13. First, mass conservation for the liquid film and the vapor core can be expressed, respectively, as:

$$\frac{d\dot{m}_f}{dz} - \Gamma_{fg} = 0, \tag{7}$$

and

$$\frac{d\dot{m}_g}{dz} + \Gamma_{fg} = 0, \tag{8}$$

where the mass flow rates of the liquid film and the vapor core, and the rate of interfacial mass transfer due to condensation are defined, respectively, as:

$$\dot{m}_f = \rho_f \int_0^{\delta} u_f \pi (D - 2y) dy, \tag{9}$$

$$\dot{m}_g = \frac{\rho_g \bar{u}_g \pi (D - 2\delta)^2}{4}, \tag{10}$$

and

$$\Gamma_{fg} = \frac{q''_w \pi D}{h_{fg}}. \tag{11}$$

Neglecting axial momentum changes in the liquid film and applying momentum conservation to the liquid film control volume illustrated in Fig. 13a yield:

$$\tau = \left(-\frac{dp}{dz} + \rho_f g\right)\frac{A_{f,*}}{P_{f,y}} + \frac{\tau_i P_{f,\delta} + \Gamma_{fg} u_i}{P_{f,y}}, \tag{12}$$

where the flow area, $A_{f,*}$, local perimeter, $P_{f,y}$, and interfacial perimeter, $P_{f,\delta}$, can be expressed, respectively, as:

$$A_{f,*} = \frac{\pi}{4}(D - 2y)^2 - \frac{\pi}{4}(D - 2\delta)^2, \tag{13}$$

$$P_{f,y} = \pi(D - 2y), \tag{14}$$

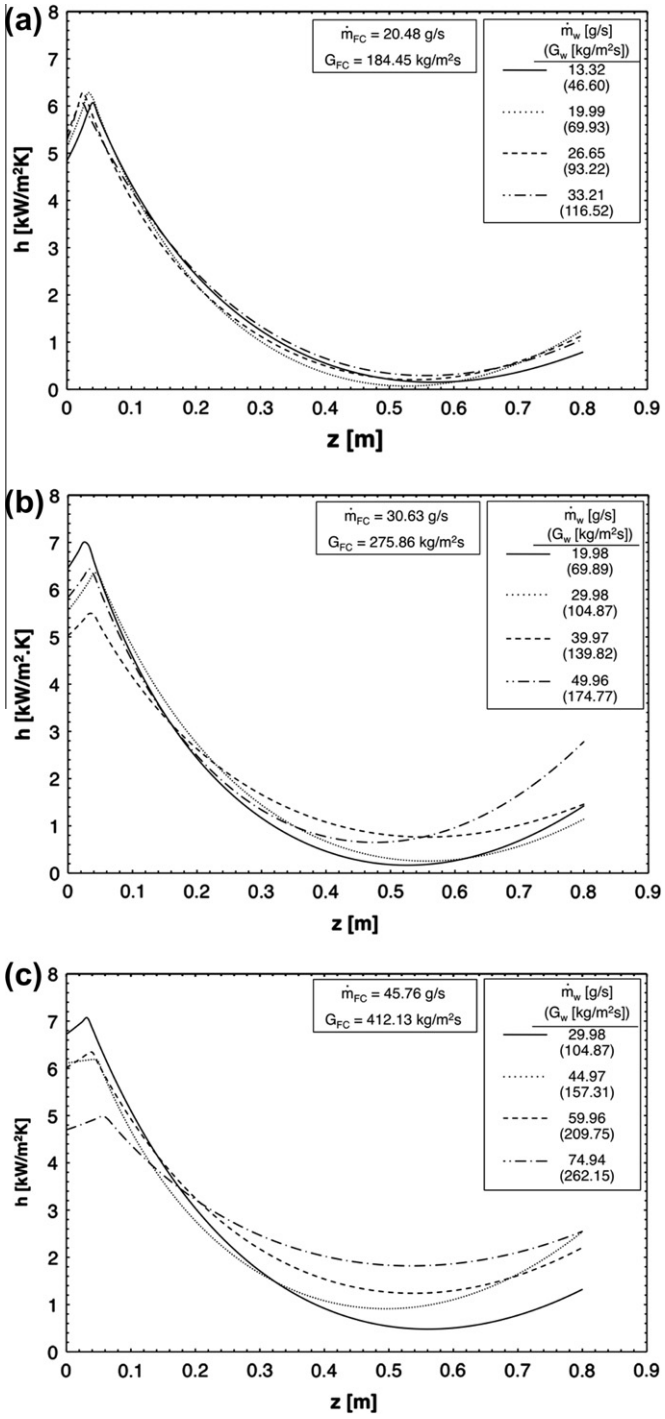

Fig. 9. Variation of experimentally determined local FC-72 condensation heat transfer coefficient with axial distance for different water flow rates and FC-72 mass flow rates of (a) 20.48 g/s (G_{FC} = 184.45 kg/m^2 s), (b) 30.63 g/s (G_{FC} = 275.86 kg/m^2 s), and (c) 45.76 g/s (G_{FC} = 412.13 kg/m^2 s).

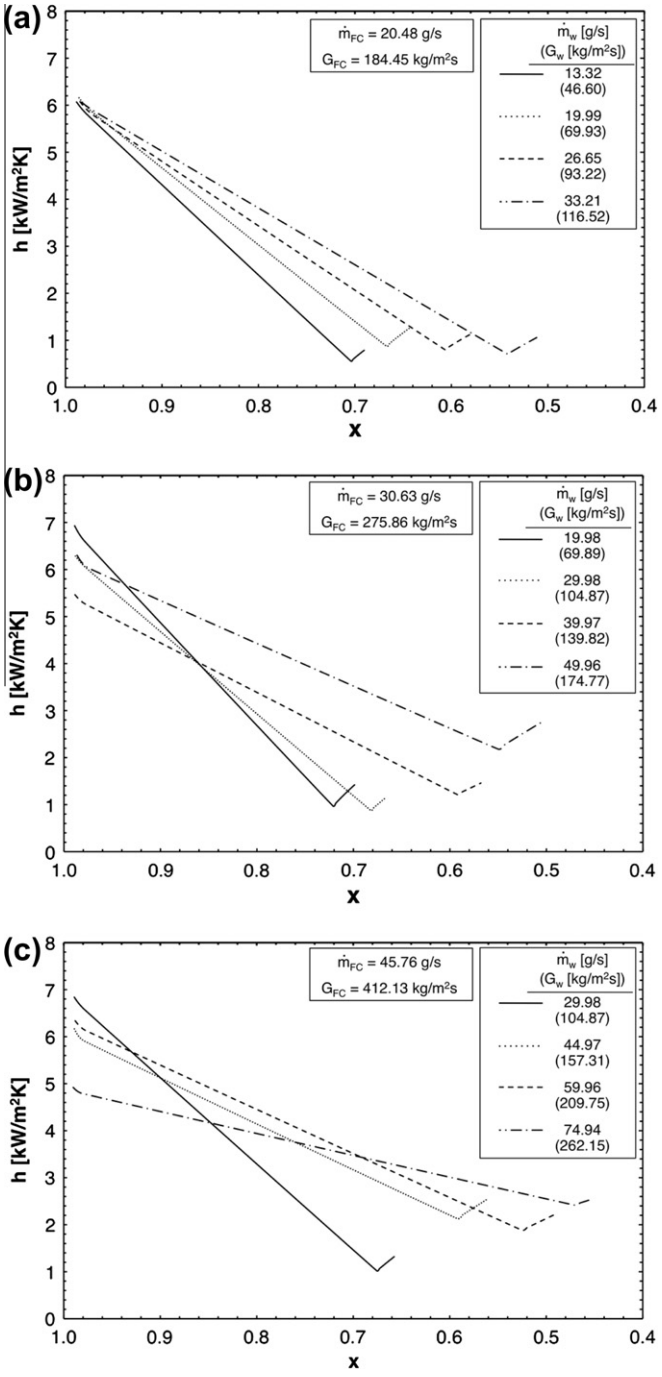

Fig. 10. Variation of experimentally determined local FC-72 condensation heat transfer coefficient with vapor quality for different water flow rates and FC-72 mass flow rates of (a) 20.48 g/s (G_{FC} = 184.45 kg/m^2 s), (b) 30.63 g/s (G_{FC} = 275.86 kg/m^2 s), and (c) 45.76 g/s (G_{FC} = 412.13 kg/m^2 s). These plots exclude the region captured in Fig. 9 from the inlet to the peak point.

and

$$P_{f,\delta} = \pi(D - 2\delta). \tag{15}$$

Allowing for turbulence in the condensing film, the shear stress in the film can be expressed as:

$$\tau = \mu_f \left(1 + \frac{\varepsilon_m}{\nu_f}\right) \frac{du_f}{dy}, \tag{16}$$

where ε_m is the eddy momentum diffusivity. Substituting Eq. (16) into Eq. (12) and integrating yield the velocity profile across the liquid film:

$$u_f(y) = \frac{\delta}{\mu_f}\left(-\frac{dP}{dz} + \rho_f g\right) \int_0^{y/\delta} \frac{A_{f,*}}{P_{f,y}} \left(1 + \frac{\varepsilon_m}{\nu_f}\right)^{-1} d\left(\frac{y}{\delta}\right) + \frac{\delta}{\mu_f}\left(\tau_i P_{f,\delta} + \Gamma_{fg} u_i\right) \int_0^{y/\delta} \frac{1}{P_{f,y}} \left(1 + \frac{\varepsilon_m}{\nu_f}\right)^{-1} d\left(\frac{y}{\delta}\right). \tag{17}$$

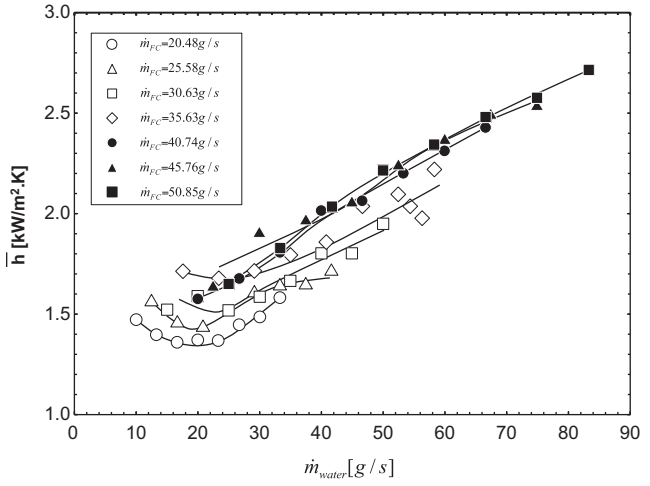

Fig. 11. Variation of experimentally determined average FC-72 condensation heat transfer coefficient with water flow rate for different FC-72 mass flow rates.

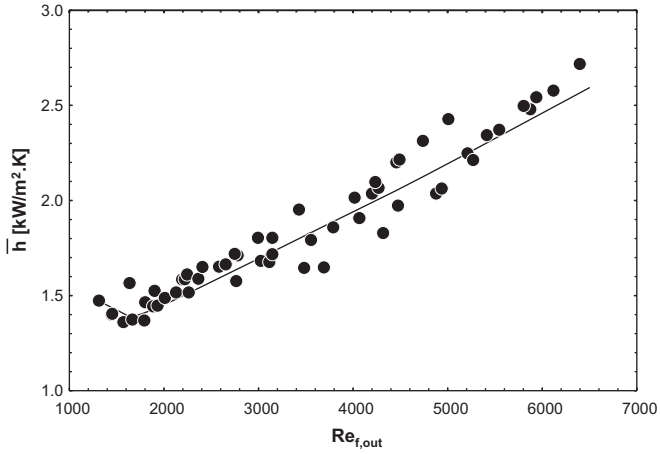

Fig. 12. Variation of experimentally determined average FC-72 condensation heat transfer coefficient with film Reynolds number at the exit.

Substituting Eq. (17) into Eq. (9) yields the following relation for pressure gradient,

$$-\frac{dP}{dz}=-\rho_f g+\frac{\frac{\mu_f \dot{m}_f}{\rho_f \delta^2}-(\tau_i P_{f,\delta}+\Gamma_{fg}u_i)\int_0^1\left[P_{f,y}\int_0^{y/\delta}\frac{1}{P_{f,y}}\left(1+\frac{\varepsilon_m}{\nu_f}\right)^{-1}d\left(\frac{y}{\delta}\right)\right]d\left(\frac{y}{\delta}\right)}{\int_0^1\left[P_{f,y}\int_0^{y/\delta}\frac{A_{f,*}}{P_{f,y}}\left(1+\frac{\varepsilon_m}{\nu_f}\right)^{-1}d\left(\frac{y}{\delta}\right)\right]d\left(\frac{y}{\delta}\right)}, \tag{18}$$

where the interfacial velocity, u_i, can be determined by setting $y = \delta$ in Eq. (17).

Applying momentum conservation to the vapor core control volume illustrated in Fig. 13b yields:

$$\tau_i=\frac{1}{P_{f,\delta}}\left[A_g\left(-\frac{dP}{dz}+\rho_g g\right)-\frac{d\left(\rho_g \bar{u}_g^2 A_g\right)}{dz}-\Gamma_{fg}u_i\right], \tag{19}$$

where the flow area of the vapor core is $A_g=\pi(D-2\delta)^2/4$.

The interfacial shear stress is the result of velocity differences between the vapor core and interface, modified by the influence of interfacial momentum transfer due to condensation; the later is obtained using a treatment by Wallis [50]:

$$\tau_i=\frac{1}{2}f_i\rho_g(\bar{u}_g-u_i)^2+\frac{(\bar{u}_g-u_i)\Gamma_{fg}}{2P_{f,\delta}}. \tag{20}$$

The interfacial friction factor, f_i, can be determined from relations by Shah and London [51],

$$f_i=16/\mathrm{Re}_c \quad \text{for } \mathrm{Re}_c<2000, \tag{21a}$$

$$f_i=0.079\mathrm{Re}_c^{-0.25} \quad \text{for } 2000\leqslant \mathrm{Re}_c<20,000, \tag{21b}$$

and

$$f_i=0.046\mathrm{Re}_c^{-0.2} \quad \text{for } \mathrm{Re}_c\geqslant 20,000, \tag{21c}$$

where Re_c is the effective vapor core Reynolds number given by:

$$\mathrm{Re}_c=\frac{\rho_g(\bar{u}_g-u_i)(D-2\delta)}{\mu_g}. \tag{22}$$

5.2. Determination of the condensation heat transfer coefficient

Heat flux across the liquid film is related to the liquid temperature gradient by the relation:

$$\frac{q''}{q''_w}=\left(\frac{1}{\mathrm{Pr}_f}+\frac{1}{\mathrm{Pr}_T}\frac{\varepsilon_m}{\nu_f}\right)\frac{dT^+}{dy^+}, \tag{23}$$

where

$$T^+=\frac{\rho_f c_{p,f}u^*(T-T_w)}{q''_w}, \tag{24}$$

$$y^+=\frac{yu^*}{\nu_f}, \tag{25}$$

$$u^*=\sqrt{\frac{\tau_w}{\rho_f}}, \tag{26}$$

and Pr_T is the turbulent Prandtl number ($\varepsilon_m/\varepsilon_h$), which, as discussed by Mudawar and El-Masri [44], can be evaluated from the experimental data of Ueda et al. [43]:

$$\mathrm{Pr}_T=1.4\exp\left(-15\frac{y^+}{\delta^+}\right)+0.66, \tag{27}$$

where

$$\delta^+=\frac{\delta u^*}{\nu_f}. \tag{28}$$

Based on Mudawar and El-Masri's turbulent mixing length profile [44], which incorporates an eddy-diffusivity profile measured by Ueda et al. [43] and Kim and Mudawar [41] derived the following form of eddy momentum diffusivity distribution in a shear-driven film (as discussed in [41], this profile is used for macro-channels, which is different from a profile they developed specifically for condensation in micro-channels)

$$\frac{\varepsilon_m}{\nu_f}=-\frac{1}{2}+\frac{1}{2}\times\sqrt{1+4K^2y^{+2}\left[1-\exp\left(-\sqrt{1-\frac{y^+}{\delta^+}}\frac{y^+}{A^+}\right)\right]^2\left(1-\frac{y^+}{\delta^+}\right)\frac{\tau}{\tau_w}}, \tag{29}$$

where the Von-Karman constant is $K = 0.4$, the constant A^+ is given by [41,44,52,53]:

$$A^+=26\left(1+30.18\mu_f\rho_f^{-0.5}\tau_w^{-1.5}\frac{dP}{dz}\right)^{-1}, \tag{30}$$

and based on Eq. (12),

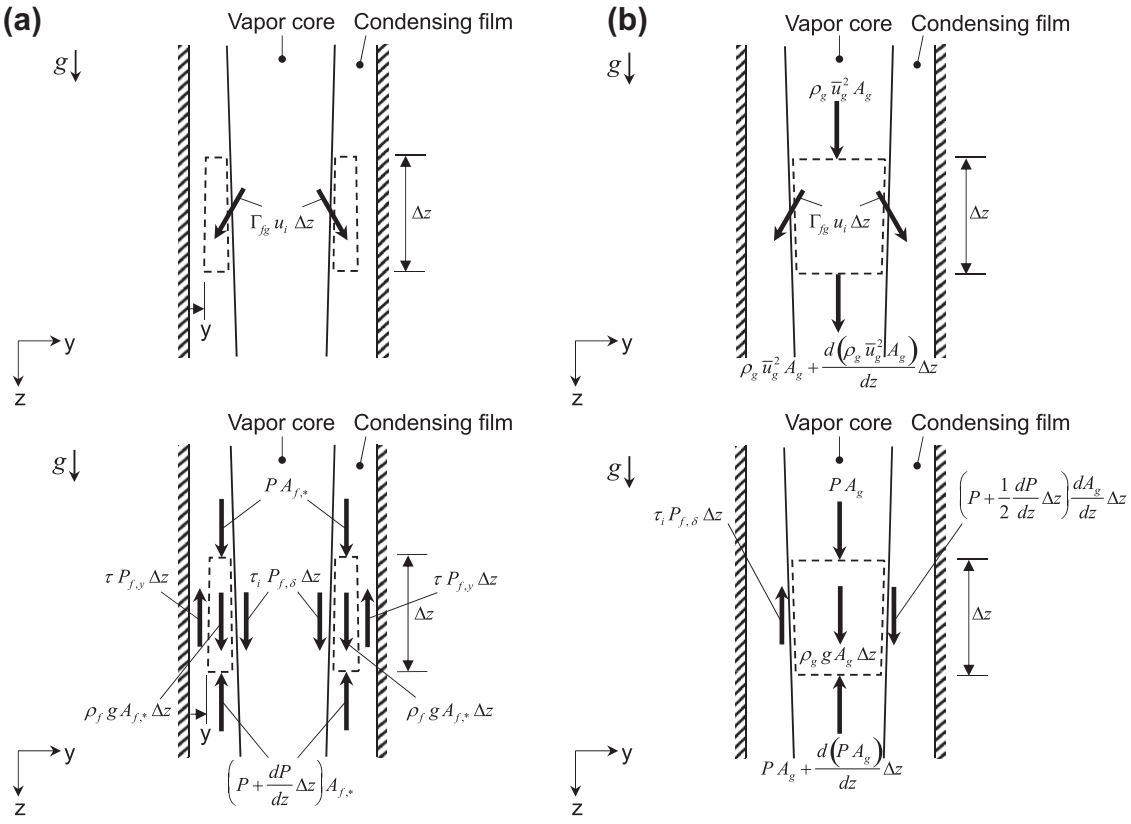

Fig. 13. Momentum and force components for (a) liquid film control volume and (b) vapor core control volume.

$$\frac{\tau}{\tau_w} = \frac{\pi D}{P_{f,y}} \frac{\left(-\frac{dP}{dz} + \rho_f g\right) A_{f,*} + \tau_i P_{f,\delta} + \Gamma_{fg} u_i}{\left(-\frac{dP}{dz} + \rho_f g\right)[\pi\delta(D-\delta)] + \tau_i P_{f,\delta} + \Gamma_{fg} u_i}. \tag{31}$$

Integrating Eq. (23), the local condensation heat transfer coefficient can be expressed as:

$$h = \frac{q''_w}{T_{sat} - T_w} = \frac{\rho_f c_{p,f} u^*}{T^+_\delta} = \frac{\rho_f c_{p,f} u^*}{\int_0^{\delta^+} \frac{q''}{q''_w}\left(\frac{1}{\mathrm{Pr}_f} + \frac{1}{\mathrm{Pr}_T}\frac{\varepsilon_m}{\nu_f}\right)^{-1} dy^+}$$
$$= \frac{\rho_f c_{p,f} u^*}{\int_0^{\delta^+} \left(\frac{D}{D-2\delta}\right)\left(\frac{1}{\mathrm{Pr}_f} + \frac{1}{\mathrm{Pr}_T}\frac{\varepsilon_m}{\nu_f}\right)^{-1} dy^+}. \tag{32}$$

To determine $h(z)$, the model equations are solved numerically using a finite difference technique. The axial distance is divided into small Δz increments and calculations are repeated until the outlet of the condensation length is reached. The average heat transfer coefficient, $\bar{h}$, for the annular region is obtained by averaging the values of $h(z)$ predicted by the model over the annular region downstream of the peak values in Fig. 9.

5.3. Model predictions

Fig. 14 compares the average heat transfer coefficient values predicted by the annular model to the experimental data. Good predictions are evidenced by a mean absolute error of 12.59%, with most of the predictions falling within ±30% of the data. This demonstrates the effectiveness of both the control volume approach and eddy diffusivity profile.

One possible reason for the slight differences between the predicted and measured values is the annular film's interfacial waviness, which is not accounted for in the model. Waviness can influence annular condensation in several ways, by increasing interfacial area, altering turbulence within the film, and causing fluctuations in film thickness with the wave peaks moving faster than the thinner substrate.

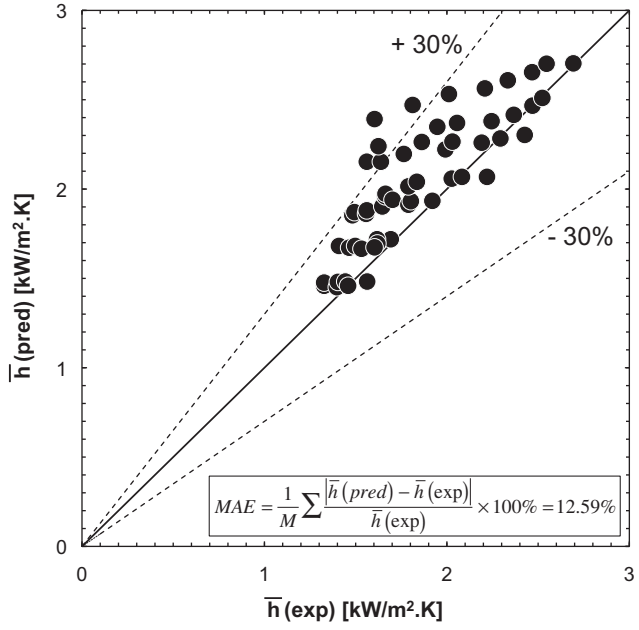

Fig. 14. Comparison of predicted and experimentally determined average condensation heat transfer coefficients.

6. Conclusions

This study investigated the interfacial and heat transfer characteristics of annular condensation of FC-72 in vertical downflow. High-speed video imaging provided valuable insight into the film's interfacial behavior for different flow rates of FC-72 and cooling water. Detailed temperature measurements enabled the determination of axial variations of the condensation heat transfer coefficient. A theoretical control-volume-based model was developed, which accounts for the influence of surface tension on turbulence in the vicinity of the interface. Key findings from the study can be summarized as follows:

(1) For very low flow rates of FC-72 and corresponding exit film Reynolds numbers below 770, the film is smooth and laminar. Increasing the flow rate of FC-72 for a fixed flow rate of the cooling water, turns the film turbulent with the interface incurring chaotic interfacial waves, especially for exit film Reynolds numbers above 1800. This behavior is largely the result of the increased interfacial shear associated with higher FC-72 flow rates.

(2) With inlet conditions slightly superheated, the measured local heat transfer coefficient is relatively low near the inlet and increases rather sharply to peak value where the annular liquid film is initiated. The heat transfer coefficient decreases axially from its peak value because of the gradual thickening of the liquid film. However, the data show a downstream minimum before increasing again towards the outlet. Two possible reasons for the downstream increase are transition from laminar to turbulent flow, and heat transfer enhancement caused by the more intense downstream waviness. Increasing the flow rate of FC-72 increases the heat transfer coefficient because of the increasing vapor shear and resulting thinning of the film. Increasing the flow rate of cooling water decreases the heat transfer coefficient upstream by hastening the condensation process and thickening the film in the upstream conduction-dominated region. However, the increase in cooling rate precipitates both an earlier transition to turbulent flow and an increase in turbulence overall, which enhance the heat transfer coefficient downstream.

(3) A new control-volume-based model is proposed for annular condensation in which mass, momentum, and energy conservation relations are applied to control volumes encompassing the liquid film and vapor core separately. The model also incorporates an eddy diffusivity profile for the liquid film that accounts for interfacial dampening of turbulence due to surface tension. The model shows good accuracy in predicting the average condensation heat transfer coefficient data in both magnitude and trend, evidenced by a mean absolute error of 12.59%. Future improvement to the model predictions is possible by addressing the influence of interfacial waves, which is not accounted for in the model.

Acknowledgement

The authors are grateful for the partial support for this Project from the National Aeronautics and Space Administration (NASA) under Grant No. NNX09AJ51A.

References

[1] T.M. Anderson, I. Mudawar, Microelectronic cooling by enhanced pool boiling of a dielectric fluorocarbon liquid, J. Heat Transfer – Trans. ASME 111 (1989) 752–759.
[2] I. Mudawar, Two-phase micro-channel heat sinks: theory, applications and limitations, J. Electron. Packag. – Trans. ASME 133 (2011). 041002-2.
[3] I. Mudawar, K.A. Estes, Optimizing and predicting CHF in spray cooling of a square surface, J. Heat Transfer – Trans. ASME 118 (1996) 672–680.
[4] L. Lin, R. Ponnappan, Heat transfer characteristics of spray cooling in a closed loop, Int. J. Heat Mass Transfer 46 (2003) 3737–3746.
[5] J.R. Rybicki, I. Mudawar, Single-phase and two-phase cooling characteristics of upward-facing and downward-facing sprays, Int. J. Heat Mass Transfer 49 (2006) 5–16.
[6] Y. Katto, M. Kunihiro, Study of the mechanism of burn-out in boiling system of high burn-out heat flux, Bull. JSME 16 (1973) 1357–1366.
[7] I. Mudawar, D.C. Wadsworth, Critical heat flux from a simulated electronic chip to a confined rectangular impinging jet of dielectric liquid, Int. J. Heat Mass Transfer 34 (1991) 1465–1480.
[8] D.C. Wadsworth, I. Mudawar, Enhancement of single-phase heat transfer and critical heat flux from an ultra-high-flux simulated microelectronic heat source to a rectangular impinging jet of dielectric liquid, J. Heat Transfer – Trans. ASME 114 (1992) 764–768.
[9] M.E. Johns, I. Mudawar, An ultra-high power two-phase jet-impingement avionic clamshell module, J. Electron. Packag. – Trans. ASME 118 (1996) 264–270.
[10] T.C. Willingham, I. Mudawar, Forced-convection boiling and critical heat flux from a linear array of discrete heat sources, Int. J. Heat Mass Transfer 35 (1992) 2879–2890.
[11] M.B. Bowers, I. Mudawar, High flux boiling in low flow rate, low pressure drop mini-channel and micro-channel heat sinks, Int. J. Heat Mass Transfer 37 (1994) 321–332.
[12] T.N. Tran, M.W. Wambsganss, D.M. France, Small circular- and rectangular-channel boiling with two refrigerants, Int. J. Multiphase Flow 22 (1996) 485–498.
[13] H.J. Lee, S.Y. Lee, Heat transfer correlation for boiling flows in small rectangular horizontal channels with low aspect ratios, Int. J. Multiphase Flow 27 (2001) 2043–2062.
[14] V. Khanikar, I. Mudawar, T. Fisher, Effects of carbon nanotube coating on flow boiling in a micro-channel, Int. J. Heat Mass Transfer 52 (2009) 3805–3817.
[15] X. Huang, G. Ding, H. Hu, Y. Zhu, H. Peng, Y. Gao, B. Deng, Influence of oil on flow condensation heat transfer of R410A inside 4.18 mm and 1.6 mm inner diameter horizontal smooth tubes, Int. J. Refrig. 33 (2010) 158–169.
[16] J.E. Park, F. Vakili-Farahani, L. Consolini, J.R. Thome, Experimental study on condensation heat transfer in vertical minichannels for new refrigerant R1234ze(E) versus R134a and R236fa, Exp. Therm. Fluid Sci. 35 (2011) 442–454.
[17] W.W. Akers, H.F. Rosson, Condensation inside a horizontal tube, Chem. Eng. Prog. Symp. 56 (1960) 145–149.
[18] A. Cavallini, R. Zecchin, A dimensionless correlation for heat transfer in forced convection condensation, in: Proc. 5th Int. Heat Transfer Conf., Tyoko, Japan, vol. 3, 1974, pp. 309–313.
[19] M.M. Shah, A general correlation for heat transfer during film condensation inside pipes, Int. J. Heat Mass Transfer 22 (1979) 547–556.
[20] H. Haraguchi, S. Koyama, T. Fujii, Condensation of refrigerants HCFC 22, HFC 134a and HCFC 123 in a horizontal smooth tube (2nd report), Trans. JSME (B) 60 (1994) 245–252.
[21] M.K. Dobson, J.C. Chato, Condensation in smooth horizontal tubes, J. Heat Transfer – Trans. ASME 120 (1998) 193–213.
[22] K.W. Moser, R.L. Webb, B. Na, A new equivalent Reynolds number model for condensation in smooth tubes, J. Heat Transfer – Trans. ASME 120 (1998) 410–417.
[23] W.W. Wang, T.D. Radcliff, R.N. Christensen, A condensation heat transfer correlation for millimeter-scale tubing with flow regime transition, Exp. Therm. Fluid Sci. 26 (2002) 473–485.
[24] S. Koyama, K. Kuwahara, K. Nakashita, K. Yamamoto, An experimental study on condensation of refrigerant R134a in a multi-port extruded tube, Int. J. Refrig. 24 (2003) 425–432.
[25] M.M. Shah, An improved and extended general correlation for heat transfer during condensation in plain tubes, HVAC&R Res. 15 (2009) 889–913.
[26] T. Bohdal, H. Charun, M. Sikora, Comparative investigations of the condensation of R134a and R404A refrigerants in pipe minichannels, Int. J. Heat Mass Transfer 54 (2011) 1963–1974.
[27] I. Mudawar, M.B. Bowers, Ultra-high critical heat flux (CHF) for subcooled water flow boiling – I. CHF data and parametric effects for small diameter tubes, Int. J. Heat Mass Transfer 42 (1999) 1405–1428.
[28] D.D. Hall, I. Mudawar, Ultra-high critical heat flux (CHF) for subcooled water flow boiling – II. High-CHF database and design parameters, Int. J. Heat Mass Transfer 42 (1999) 1429–1456.
[29] D.D. Hall, I. Mudawar, Critical heat flux (CHF) for water flow in tubes – I. Compilation and assessment of world CHF data, Int. J. Heat Mass Transfer 43 (2000) 2573–2604.
[30] D.D. Hall, I. Mudawar, Critical heat flux (CHF) for water flow in tubes – II. Subcooled CHF correlations, Int. J. Heat Mass Transfer 43 (2000) 2605–2640.
[31] S.M. Kim, I. Mudawar, Universal approach to predicting two-phase frictional pressure drop for adiabatic and condensing mini/micro-channel flows, Int. J. Heat Mass Transfer 55 (2012) 3246–3261.

[32] S.M. Kim, I. Mudawar, Universal approach to predicting heat transfer coefficient for condensing mini/micro-channel flows, Int. J. Heat Mass Transfer 56 (2013) 238–250.
[33] I. Mudawar, A.H. Howard, C.O. Gersey, An analytical model for near-saturated pool boiling CHF on vertical surfaces, Int. J. Heat Mass Transfer 40 (1997) 2327–2339.
[34] A.H. Howard, I. Mudawar, Orientation effects on pool boiling CHF and modeling of CHF for near-vertical surfaces, Int. J. Heat Mass Transfer 42 (1999) 1665–1688.
[35] J.E. Galloway, I. Mudawar, CHF mechanism in flow boiling from a short heated wall-part 1. Examination of near-wall conditions with the aid of photomicrography and high-speed video imaging, Int. J. Heat Mass Transfer 36 (1993) 2511–2526.
[36] J.E. Galloway, I. Mudawar, CHF mechanism in flow boiling from a short heated wall-part 2. Theoretical CHF model, Int. J. Heat Mass Transfer 36 (1993) 2527–2540.
[37] C.O. Cersey, I. Mudawar, Effects of heater length and orientation on the trigger mechanism for near-saturated flow boiling critical heat flux – I. Photographic study and statistical characterization of the near-wall interfacial features, Int. J. Heat Mass Transfer 38 (1995) 629–641.
[38] C.O. Cersey, I. Mudawar, Effects of heater length and orientation on the trigger mechanism for near-saturated flow boiling critical heat flux – II. Critical heat flux model, Int. J. Heat Mass Transfer 38 (1995) 643–654.
[39] J.C. Sturgis, I. Mudawar, Critical heat flux in a long, rectangular channel subjected to onesided heating – I. Flow visualization, Int. J. Heat Mass Transfer 42 (1999) 1835–1847.
[40] J.C. Sturgis, I. Mudawar, Critical heat flux in a long, rectangular channel subjected to onesided heating – II. Analysis of critical heat flux data, Int. J. Heat Mass Transfer 42 (1999) 1849–1862.
[41] S.M. Kim, I. Mudawar, Theoretical model for annular flow condensation in rectangular micro-channels, Int. J. Heat Mass Transfer 55 (2012) 958–970.
[42] G.L. Hubbard, A.F. Mills, D.K. Chung, Heat transfer across a turbulent falling film with cocurrent vapor flow, J. Heat Transfer – Trans. ASME 98 (1976) 319–320.
[43] H. Ueda, R. Moller, S. Komori, T. Mizushima, Eddy diffusivity near the free surface of open channel flow, Int. J. Heat Mass Transfer 20 (1977) 1127–1136.
[44] I. Mudawar, M.A. El-Masri, Momentum and heat transfer across freely-falling turbulent liquid films, Int. J. Multiphase flow 12 (1986) 771–790.
[45] J.A. Shmerler, I. Mudawar, Local heat transfer coefficient in wavy free-falling turbulent liquid films undergoing uniform sensible heating, Int. J. Heat Mass Transfer 31 (1988) 67–77.
[46] J.A. Shmerler, I. Mudawar, Local evaporative heat transfer coefficient in turbulent free-falling liquid films, Int. J. Heat Mass Transfer 31 (1988) 731–742.
[47] T.H. Lyu, I. Mudawar, Statistical investigation of the relationship between interfacial waviness and sensible heat transfer to a falling liquid film, Int. J. Heat Mass Transfer 34 (1991) 1451–1464.
[48] I. Mudawar, R.A. Houpt, Measurement of mass and momentum transport in wavy-laminar falling liquid films, Int. J. Heat Mass Transfer 36 (1993) 4151–4162.
[49] J.E. Koskie, I. Mudawar, W.G. Tiederman, Parallel-wire probes for measurement of thick liquid films, Int. J. Multiphase Flow 15 (1989) 521–530.
[50] G.B. Wallis, One-dimensional Two-phase Flow, McGraw-Hill, New York, 1969.
[51] R.K. Shah, A.L. London, Laminar Flow Forced Convection in Ducts: A Source Book for Compact Heat Exchanger Analytical Data, Academic Press, New York, 1978.
[52] W.M. Kays, Heat-transfer to transpired turbulent boundary-layer, Int. J. Heat Mass Transfer 15 (1972) 1023–1044.
[53] W.M. Kays, M.E. Crawford, Convective Heat and Mass Transfer, second ed., McGraw-Hill, New York, 1980.